J. Fluid Mech. (1992), *vol.* 234, *pp.* 393–416
Printed in Great Britain

Transition from hexagons to rolls in convection in fluids under non-Boussinesq conditions

By E. PAMPALONI[1], C. PÉREZ-GARCÍA[2]†, L. ALBAVETTI[1] AND S. CILIBERTO[1]

[1] Istituto Nazionale di Ottica, Largo Enrico Fermi 6, 50125 Arcetri-Firenze, Italia

[2] Departamento de Física, Universidad de Navarra, 31080 Pamplona, Navarra, Spain

(Received 7 May 1990 and in revised form 11 June 1991)

The transition between hexagons and rolls in convective patterns has been studied. The transition thresholds and changes in the Nusselt number are discussed theoretically in terms of calculations made by Busse (1967*a*) and with amplitude equations. Experiments have been done in a shallow layer of pure water under non-Boussinesq conditions using complementary techniques: shadowgraph (qualitative), optical (based on the deflections of a laser beam) and calorimetric. The experimental values of the critical Rayleigh number R_c and the critical wavenumber k_c are in agreement with theoretical ones. However, theory and experiments show some discrepancies in the slopes of the non-dimensional convective heat flow curve and in the thresholds of the hysteretic hexagons–rolls transition. These discrepancies are discussed in terms of lateral effects and of the presence of defects in the pattern.

1. Introduction

Rayleigh–Bénard convection provides a good example of dynamical pattern-forming systems. When the driving control parameter exceeds a critical value, a homogeneous translationally invariant state loses stability. In the case of Rayleigh–Bénard (RB) convection this corresponds to the rest state, which is replaced by motions that organize themselves to form a pattern of rolls. However, by considering temperature-dependent transport coefficients (non-Boussinesq conditions) (Palm 1960; Busse 1967*a*; Hoard, Robertson & Acrivos 1970; Dubois, Bergé & Wesfreid 1978; Ciliberto, Pampaloni & Pérez-Garcia 1988), patterns of hexagons can appear.

At a secondary threshold a transition between different symmetries is also possible. This is not the same case as in an order–disorder transition but is more similar to a first-order phase transition with a gap in the order parameter. In these non-equilibrium transitions the state with higher symmetry (hexagons) is replaced by one with lower symmetry (rolls). Some weakly nonlinear theoretical analyses predict that hexagons can become unstable against rolls after some secondary threshold in simple liquids under non-Boussinesq conditions (Palm 1960; Busse 1967*a*). Experiments (Dubois *et al.* 1978; Walden & Ahlers 1981; Ciliberto *et al.* 1988) support this result.

Heat flow measurements can characterize globally these transitions because this quantity is sensitive to the symmetry variations. In fact, the slope of the curve of the

† Also at Department de Física, Universitat Autònoma de Barcelona, 08193 Bellaterra (Barcelona), Catalonia, Spain.

non-dimensional convective heat flow $\mathcal{N}$ (proportional to the ratio between the convective heat flow and the conductive one) changes for different symmetries as calculated by Schlüter, Lortz & Busse (1965) and shown experimentally by Walden & Ahlers (1981). Therefore, the calorimetric technique is a suitable method to survey global changes in the pattern. Other kinds of techniques can be used to characterize these transitions. Dubois *et al.* (1978) used laser-Doppler anemometry in the transition from hexagons to rolls in water near 4 °C (non-Boussinesq conditions). Another very useful technique has been recently used by Ciliberto *et al.* (1988) to study this transition.

Usually an important difference between theory and experiments in pattern-forming systems arises as a consequence of the finite extent of real systems. Theoretical studies deal with the case of an infinite aspect ratio Γ (the ratio between a characteristic horizontal length and the layer thickness), while in experiments lateral boundaries introduce important effects. The first effect is the modification of the temperature difference at the convective threshold (Charlson & Sani 1970; Brown & Stewartson 1977). The second important effect of lateral walls is a wavenumber selection mechanism that has been studied by Cross *et al.* (1980). When the selected wavenumber does not coincide with the critical one, i.e. that obtained by the linear theory for an infinite system, the non-dimensional convective heat flow $\mathcal{N}$ is modified. Therefore, to understand the transition between different planforms it is very important to know the variation in the wavenumber (see the extensive study of Walden *et al.*).

The third effect is due to defects that, although local, lead to global changes in the pattern introducing disorder even near threshold (see Heutmaker & Gollub 1987; Steinberg, Ahlers & Cannell 1985). The dynamics of defects in convective patterns of rolls have been extensively studied (Manneville 1990). In hexagonal patterns the main defect is the pentagon–heptagon pair (Pantaloni & Cerisier 1983), which introduces dislocations in two of the three directions that form the hexagonal lattice. Therefore, in a transition between different symmetries defects play an important role similar to that of condensation nuclei in first-order phase transitions in equilibrium. Of course, the presence of these defects modifies the transition thresholds.

The purpose of the present paper is to analyse in some detail the characteristic of the transition between hexagons and rolls in convection in fluids under non-Boussinesq conditions. Section 2 is devoted to discussing some of the theoretical tools to relate the amplitude equations with the heat flow measurements. In §3 we describe in some detail the experimental set-up and techniques. In §4 the transition between hexagons and rolls is analysed, and a comparison between theory and experiment is made. Finally conclusions are presented in §5.

2. Some theoretical tools to study convection under non-Boussinesq conditions

2.1. *Calculation of the critical Rayleigh number in finite geometries*

The most relevant parameters in RB convection are the Rayleigh number $R = \alpha g \Delta T d^3/\nu\kappa$, the relation between buoyancy effects and dissipative effects, and the Prandtl number $Pr = \nu/\kappa$, the ratio between vorticity and heat diffusion coefficients. In the present definitions the parameters α, g, ν and κ correspond to the thermal expansion coefficient, the acceleration due to gravity, the kinematic viscosity and the heat diffusivity.

In the Oberbeck–Boussinesq (OB) approximation theoretical calculations show that convection starts for $R \geqslant R_c = 1708$ (the subscript c denotes critical values at threshold) for $\Gamma = \infty$ (Chandrasekhar 1961). However, some corrections must be added to take into account the finite size, the geometry and the departures from the OB approximation. Some authors have discussed theoretically the influence of the geometry on the onset of convection (Davis 1967; Davis-Jones 1970; Catton 1970; Wesfreid *et al.* 1978; Luijkx & Platten 1981; Ahlers *et al.* 1981). But for the cylindrical geometry and axisymmetric flow between insulating lateral walls Charlson & Sani (1970) have shown that the effects of a finite Γ obey a relation of the form

$$\epsilon_c \equiv \frac{R_c(\Gamma) - R_c(\infty)}{R_c(\infty)} = \pi^2 \xi_0^2 / 4\Gamma^2, \tag{2.1}$$

where ξ_0^2 is the correlation length in the amplitude equation (Wesfreid *et al.* 1978). For rigid–rigid boundary conditions $\xi_0^2 = 0.148$. Experimental studies show a very good agreement with (2.1) in the range of small and intermediate Γ (for a more detailed discussion on this point see §7 in Behringer & Ahlers 1982). In our case $\epsilon_c = 9.3 \times 10^{-4}$, which leads to $R_c(\Gamma = 20) = 1710$. However, corrections due to the finite thermal conductivity of the upper plate (the ratio σ of the heat conductivities of sapphire and water is $\sigma = 54$) must also be taken into account to calculate the convective threshold (Rihai 1985; Jenkins & Proctor 1984). These corrections give ΔR_c ($\sigma = 54$) ≈ -2. Therefore the corrections due to the finite size and the finite conductivity of the upper plate cancel and we recover the value $R_c = 1708$.

2.2. *Departures from the Oberbeck–Boussinesq approximation*

Convective motions are usually described under an approximation due to Oberbeck and Boussinesq. In this approximation the temperature dependence of the fluid parameters is neglected, except for the thermal expansion effect responsible for buoyancy. In the energy balance equation the viscous dissipation term is also neglected in comparison with the conductive term. There are some theoretical investigations on the effects of departures from the Oberbeck–Boussinesq approximation (Palm 1960; Segel & Stuart 1962; Segel 1965; Palm, Elligsen & Gjevik 1967; Busse 1967*a*; Davis & Segel 1968). Of these, the work of Busse (1967*a*) is the most complete because he considers the effect of small variations of all the temperature-dependent fluid parameters and the effect of the Prandtl number in a coherent manner. However, Busse's analysis (see the Appendix) has three important limitations: (i) it is calculated for a infinitely extended fluid layer and, therefore, does not include the sidewall effects; (ii) it is a purely global analysis and cannot account for the local dynamics in a pattern with defects or for the coexistence of two symmetries, usually seen in patterns with this kind of competition; (iii) the non-Boussinesq parameter is not given as a function of the Prandtl number in the rigid–rigid case (this last limitation introduces an indeterminacy in the transition threshold calculation). Experiments partially confirm some of the predictions of Busse's theoretical work (Sommerscales & Dougherty 1970; Hoard *et al.* 1970; Richter 1978; Dubois *et al.* 1978; Ahlers 1980; Behringer & Ahlers 1982; Koschmieder & Campbell 1987).

2.3. *Amplitude equations*

A more general method to study the characteristics of the hexagon–roll transition is based on the so-called amplitude equations. In the past few years numerous work has shown the validity and richness of this method that allows the main features of

pattern forming systems to be understood (Manneville 1990). This method allows local spatial variations to be accounted for (Newell & Whitehead 1969; Segel 1969) and therefore, the dynamics of defects to be studied. As we will see, the global features of the pattern can be also recovered from these equations by some integration.

The solutions of the hydrodynamic equations can be written in the form (Ahlers *et al.* 1981)

$$V(\boldsymbol{r},z,t)=\begin{pmatrix}\boldsymbol{u}(\boldsymbol{r},z,t)\\ w(\boldsymbol{r},z,t)\\ T(\boldsymbol{r},z,t)\end{pmatrix}\approx\left[\frac{R_c}{\langle w_0\theta_0\rangle_z}\right]^{\frac{1}{2}}\begin{pmatrix}\nabla\Psi(\boldsymbol{r},t)\,\boldsymbol{u}_0(z)\,\kappa/d\\ \Psi(\boldsymbol{r},t)\,w_0(z)\,\kappa/d\\ \Psi(\boldsymbol{r},t)\,\theta_0(z)\,\Delta T_c/R_c\end{pmatrix}, \tag{2.2}$$

where $\boldsymbol{r}$ is the vector in the horizontal plane and $\boldsymbol{u}(\boldsymbol{r},z,t)$, $w(\boldsymbol{r},z,t)$ and $T(\boldsymbol{r},z,t)$ denote the horizontal and the vertical components of the velocity field and the temperature field, respectively. The subcript 0 indicates the linear solution of the corresponding quantity. The order parameter $\Psi(\boldsymbol{r},t)$ is the projection of the hydrodynamical variables onto the slowest unstable mode. (The linear solutions $\boldsymbol{u}_0(z)$, $w_0(z)$ and $\theta_0(z)$, as well as the critical wavenumber $k_c=3.1$, are given in Cross 1980). The development in normal modes of this order parameter can be written as

$$\Psi(\boldsymbol{r},t)=\sum_k \psi_k \exp(\mathrm{i}\boldsymbol{k}\cdot\boldsymbol{r}), \tag{2.3}$$

where ψ_k is the Fourier coefficient of Ψ corresponding to the wavenumber $\boldsymbol{k}$.

The multiplicative factor in (2.2) has been chosen in order to have the following normalization relation:

$$\mathcal{N}\equiv\frac{(N-1)R}{R_c}=\frac{1}{S}\int\mathrm{d}x\,\mathrm{d}y\,\Psi^2=\sum_k|\psi_k|^2, \tag{2.4}$$

where $N=q_{\mathrm{tot}}/q_{\mathrm{cond}}$ is the Nusselt number, the ratio between the total heat flow $q_{\mathrm{tot}}=q_{\mathrm{cond}}+q_{\mathrm{conv}}$ and the conductive heat flow q_{cond}, and S the horizontal area of the layer. Therefore, the non-dimensional convective heat flow $\mathcal{N}$ is the sum of the intensities of all the modes present in the system.

Experimentally one can see that the convective patterns are very ordered, with a predominant geometry (rolls, hexagons, etc.). This means that the modes in the development (2.3) are concentrated into sharp peaks (two for rolls and six for hexagons) in Fourier space. Therefore, it is useful to consider the following development for the order parameter:

$$\psi(\boldsymbol{r},t)=\sqrt{2}\,\mathrm{Re}\left[\sum_{i=1}^{3}A_i(\boldsymbol{r},t)\exp(\mathrm{i}\boldsymbol{k}_i\cdot\boldsymbol{r})\right], \tag{2.5}$$

where we take as reference the hexagonal form, which is formed by the superposition of three sets of straight rolls characterized by wavenumbers that obey $\sum\boldsymbol{k}_i=0$, $|\boldsymbol{k}_i\cdot\boldsymbol{k}_j|=\frac{1}{2}k_c^2$ $(i\neq j)$ and $i=1,2,3$, and by amplitudes A_i defined as

$$A(\boldsymbol{r},t)=\sqrt{2}\left[\sum_{k\approx k_i}\psi_k\exp(\mathrm{i}(\boldsymbol{k}-\boldsymbol{k}_i)\cdot\boldsymbol{r})\right]. \tag{2.6}$$

The sum is over the modes inside a peak centred over the wavenumber $\boldsymbol{k}_i$ in the Fourier space.

The evolution of these amplitudes must be in the form

$$\tau_0 \frac{\partial A_i}{\partial t} = \left\{\epsilon + \xi_0^2 \left[\frac{\partial}{\partial x_i} - \frac{\mathrm{i}}{2k_c}\frac{\partial^2}{\partial y_i^2}\right]^2\right\} A_i + aA_{i+1}^* A_{i+2}^* - b\left[\sum_{i \neq j} |A_j|^2\right] A_i - c|A_i|^2 A_i$$

$$(i = i \bmod 3). \quad (2.7)$$

Here $\epsilon = (\Delta T - \Delta T_c)/\Delta T_c$ denotes the temperature difference above threshold. The relaxation time τ_0, the correlation length ξ_0 (which also appears in (2.1)), the critical Rayleigh number R_c and wavenumber k_c are obtained from a linear stability analysis of the full hydrodynamic equations of the system. The superscript * denotes the complex conjugate and $\partial/\partial x_i$ and $\partial/\partial y_i$ are the spatial derivatives parallel and perpendicular to the vector $\boldsymbol{k}_i$, respectively. The physical meaning of the nonlinear coefficients a, b and c, will be specified later on.

These equations can be written in a variational form (Pérez-García, Pampaloni & Ciliberto 1990*a*) and, as a consequence, the evolution of the system to stationary states is monotonic. (For a discussion of the limitations of such a variational formulation see Heutmaker & Gollub 1987.)

The stable, stationary and homogeneous solutions of (2.7) are (i) a pattern of rolls $|A_r| = |A_1| \neq 0$, $|A_2| = |A_3| = 0$, and (ii) a pattern of hexagons $|A_1| = |A_2| = |A_3| = |A_h|$. A linear stability analysis of these solutions allows it to be determined that rolls are stable for $\epsilon \geqslant \epsilon_r$, where ϵ_r is given by

$$\epsilon_r = \frac{R_r - R_c}{R_c} = \frac{a^2 b}{(b-c)^2}. \quad (2.8)$$

On the other hand, hexagons are stable in the interval $\epsilon_a \leqslant \epsilon \leqslant \epsilon_h$ with

$$\epsilon_a = \frac{R_a - R_c}{R_c} = -\frac{a^2 c}{4(2b+c)^2}, \quad \epsilon_h = \frac{R_h - R_c}{R_c} = \frac{a^2(b+2c)}{(b-c)^2}, \quad (2.9)$$

and the ratio between the two thresholds ϵ_h and ϵ_r is

$$\frac{\epsilon_h}{\epsilon_r} = \frac{b+2c}{c}. \quad (2.10)$$

The corresponding bifurcation diagram is plotted in figure 1.

It is interesting to relate the amplitude equations with the heat flow measurements. The comparison can be made by taking into account the following relation obtained by substitution of (2.5) in (2.4):

$$\mathcal{N} \equiv \frac{(N-1)R}{R_c} = \frac{1}{S}\int \mathrm{d}x\,\mathrm{d}y \sum_{i=1}^{3} |A_i|^2 = \sum_{i=1}^{3} \langle |A_i|^2 \rangle_{x,y}, \quad (2.11)$$

where the bracket $\langle\ \rangle_{x,y}$ indicates the average on the horizontal plane.

For an homogeneous hexagonal pattern the non-dimensional convective heat flow $\mathcal{N}$ is

$$\mathcal{N}_h = 3|A_h|^2 = 3/C\{a^2/2C + \epsilon + a/2C\,(a^2 + 4C\epsilon)^{\frac{1}{2}}\}, \quad (2.12)$$

where $C = c + 2b$. For rolls the expression is simply

$$\mathcal{N}_r = |A_r|^2 = \epsilon/c. \quad (2.13)$$

As a consequence the slope of $\mathcal{N}_r(\epsilon)$ gives direct information about the coefficient c, while the determination of b and a from $\mathcal{N}_h$ requires a more delicate fitting.

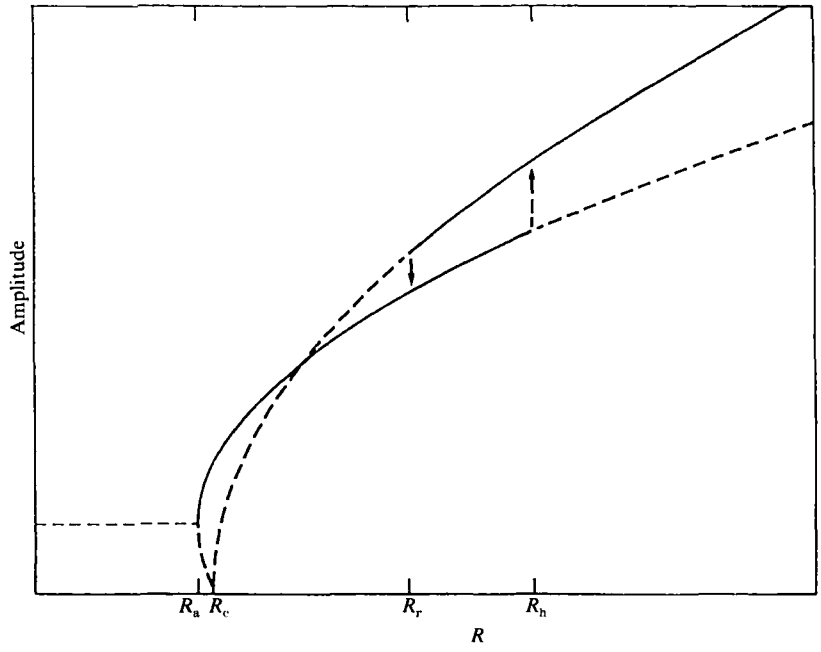

FIGURE 1. The amplitude of convective motions as a function of R. (Full lines = stable solutions, dashed lines = unstable solutions.)

3. Experimental set-up and procedure

3.1. *Characteristics of the convective fluid*

The working fluid is pure water. We gather together in table 1 the values of the different parameters of the fluid at the maximum (bottom), mean, and minimum (top) temperatures on the cell at threshold. This allows calculation of the non-dimensional numbers (Rayleigh number R, Prandtl number Pr and a non-Boussinesq parameter $\mathscr{P}$) that characterize convection and the departures from the Boussinesq approximation.

3.2. *The convective cell*

The experiment was performed in a cylindrical cell whose inner lateral wall is not vertical, but has a triangular shape in order to reduce the induction of concentric rolls due to the cylindrical symmetry. The radius at the top of the wall is $r = 36$ mm, that at the bottom is $r_b = 38$ mm and the cell depth is $d = 1.8$ mm. Consequently the aspect ratio is $\Gamma = r/d = 20$. The horizontal diffusion time is $\tau_h = r^2/\kappa = 2.45$ h.

A schematic representation of the cell and the thermal stabilization apparatus is shown in figure 2. The cell is constructed from a copper bottom plate (CP), a sapphire upper plate (SP) and a lateral wall made from Plexiglas (LW). The copper plate has its upper surface polished to a mirror finish and covered with nickel and gold films. This plate has two small holes (0.8 mm ∅) drilled on its diameter at a distance of 75 mm from each other, so these holes are just below the triangular shaped walls. An electrical resistor (ER), fed by a power supply unit (PS2), heats the bottom of the copper plate. The sapphire plate is cooled by a temperature-stabilized water flow (WF1) circulating between this plate and an upper glass plate (GP).

The cell is inside a box whose temperature is regulated by a water flow (WF2) coming from a thermal bath (TB) (Haake F3-K). By means of a heat exchanger (HE)

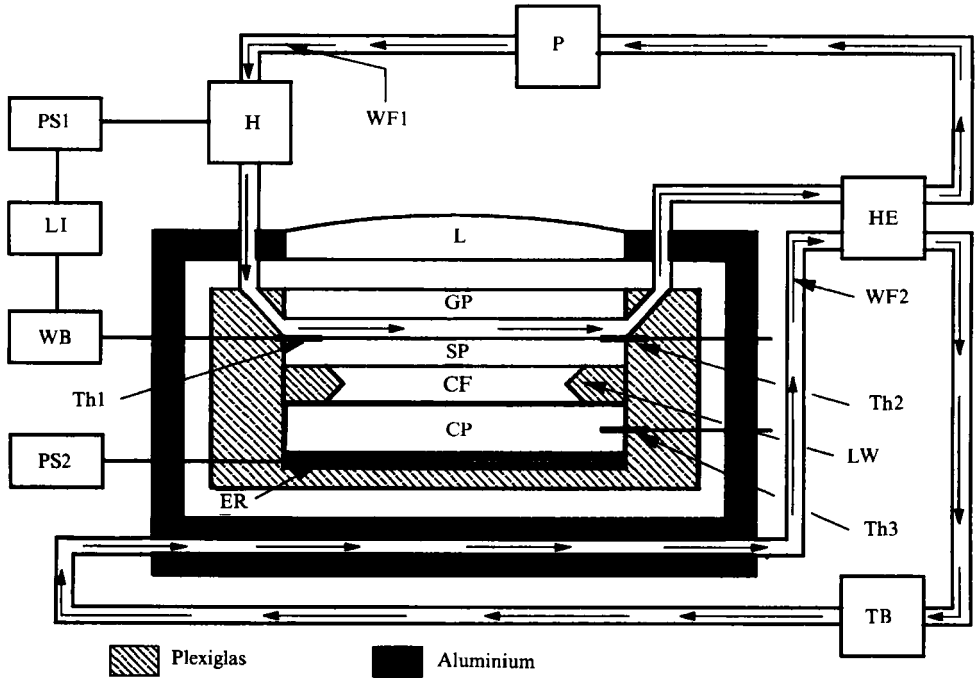

FIGURE 2. Schematic view of the convective cell and thermal regulation system: CF, convective fluid; CP, copper plate; ER, electrical resistor; GP, glass plate; H, heater; HE, heat exchanger; L, lens; LI, lock-in; LW, lateral wall; P, pump; PS1(2), power supply 1(2); SP, sapphire plate; TB, thermal bath; Th1(2, 3), thermistor 1(2, 3); WB, Wheastone bridge; WF1(2), water flow 1(2).

Water	22 °C	28.3 °C	34.6 °C
ρ (g cm^{-3})	0.99777	0.99662	0.99417
α (K^{-1})	227.5×10^{-6}	288.0×10^{-6}	342.4×10^{-6}
λ (W cm^{-1} K^{-1})	6.01×10^{-3}	6.11×10^{-3}	6.20×10^{-3}
C_p (J g^{-1} K^{-1})	4.1808	4.1787	4.1782
κ (cm^2 s^{-1})	1.44×10^{-3}	1.47×10^{-3}	1.49×10^{-3}
ν (cm^2 s^{-1})	9.569×10^{-3}	8.301×10^{-3}	7.295×10^{-3}
n	1.33281	1.33215	1.33127

TABLE 1. Water properties (ρ = density, α = thermal expansion coefficient, λ = heat conductivity, C_p = specific heat, κ = heat diffusivity, ν = kinematic viscosity and n = index of refraction) from Weast (1985)

this bath also cools the refrigerating water flow (WF1) circulated by a pump (P) (flow rate 20 dm^3/min) in the thermal stabilization circuit of the sapphire plate (SP). The thermal stability of WF1 is controlled by a feedback loop. The sensitive element of this loop is a thermistor (Th1) that measures the temperature of the top surface of the sapphire plate (SP). This thermistor is inserted in an a.c. bridge circuit (WB). The unbalance signal of the bridge circuit goes to a vectorial lock-in amplifier (LI) (EG&G PARC model 5102) that drives an external voltage-controlled power supply unit (PS1). This power unit (PS1) feeds the heater (H) that heats the water flow (WF1), thus closing the feedback loop. The measured long-term stability (one week) of the temperature of the upper plate is ± 0.005 K. The temperature difference across the

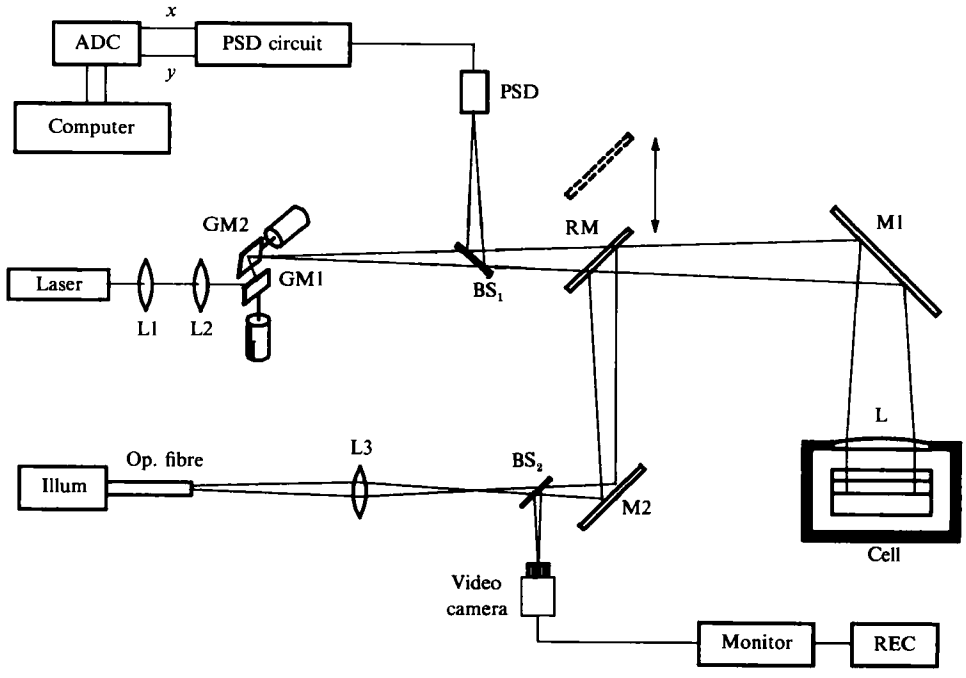

FIGURE 3. Optical set-up for the shadowgraph and the laser beam deflection techniques: BS1(2), beam splitter 1(2); GM1(2), galvanometric mirror 1(2); L, lens; L1(2, 3), lens 1(2, 3); M1(2), mirror 1(2); PSD, photo-sensitive detector; RM, removable mirror.

cell is measured with a thermistor (Th2) placed on the upper surface of the sapphire plate and another thermistor (Th3) placed in the middle of the copper plate.

3.3. *Experimental techniques*

The convective motions are analysed by three experimental techniques: shadowgraph, laser beam deflection and calorimetric.

3.3.1. *Shadowgraph technique*

The sapphire at the top of the convective cell allows optical inspection. Therefore, we can visualize the flow by vertical shadowgraph. In our case this technique only serves to give the qualitative features of the convective patterns because, as we will show in the following, the laser beam deflection is a more powerful technique for quantitative measurements. The shadowgraph method is shown in figure 3. During each of these shadowgraph measurements the removable mirror (RM) has to rest down. The light coming from an optical fibre is used as a point source, that is in the focus of the lens L3. The light passes through two lenses (L3) and (L) placed in a confocal configuration. Thus, a parallel light beam crosses the convective fluid vertically and is reflected by the polished bottom plate. The light coming back from the cell is reflected by the beam splitter (BS2) into a 50 mm objective, used to form the image of the convective pattern on a CCD video camera (SONY AVC-D5CE). This image is displayed in real time on a video monitor and recorded by a video-recorder (SONY VO-5630).

The method relies upon the variation of the index of refraction with temperature. Light rays passing through cold, dense, descending fluid are slightly focused while those crossing warm, ascending fluid are defocused. Thus, the convective motions act like thermal lenses (convergent in descending cold motion and divergent in ascending

warm motion). Therefore, one can see an image formed by dark and light regions which delineates the cells of the convective pattern. In our case the contrast between these regions is sufficient to be seen directly by sight. Although the images obtained were quite good we used an image processing system to enhance the contrast.

3.3.2. *Laser deflection technique*

This local technique (Giglio & Vendramini 1975, 1977) is based on the deflection of a laser beam that crosses the convective fluid layer along the vertical. (The method described here, is an improvement of a technique developed by Ciliberto, Francini & Simonelli 1985). This deflection is due to the gradients of the refractive index induced by the temperature field associated with the convective motions. For small deviations (typically 10^{-3} rad in our case) the deflection angles along $x(\theta_x)$ and $y(\theta_y)$ are related to the horizontal thermal gradient inside the fluid by the following expressions:

$$\theta_x = 2d\,\mathrm{d}n/\mathrm{d}T\langle\partial T/\partial x\rangle_z, \quad \theta_y = 2d\,\mathrm{d}n/\mathrm{d}T\langle\partial T/\partial y\rangle_z, \tag{3.1}$$

where $\langle\ \rangle_z$ indicates the average in the vertical direction.

The laser beam (Melles-Griot 05 LHR 121 He-Ne laser) sweeps the maximal square area inscribed in the circumference of the cell in the (x, y)-plane and so we can measure the horizontal temperature gradient averaged along z as a function of x and y. In our experimental set-up, shown in figure 3, the sweep is similar to a TV raster scan. The scanning mechanism is constructed with the two mirrors (GM1) and (GM2) mounted on two galvanometers (General Scanning G120 DCM), for the x and y scans, respectively. The lenses (L1) and (L2) focus the laser beam into the cell to have the minimum spot size (laser beam width about 0.3 mm) in the testing region.

During each of these measurements the removable mirror (RM) has to rest up. The two mirrors (GM1), (GM2) are placed very close to each other and they are (neglecting the distance between them) in the focus of the lens (L). With this arrangement the laser beam deflected by the two mirrors reaches the convective fluid remaining parallel to the optimal axis, in every position of the two-dimensional sweep, within a small error (less than 0.5 mrad). This small error is mainly due to the distance between (GM1) and (GM2), which prevents a perfect focusing of both mirrors. This error and those due to unavoidable alignment errors, optical aberrations, etc., can be corrected by subtracting a reference image (at $\Delta T = 0$) in the reconstruction of the temperature gradient field.

The sweeping laser beam, after crossing the fluid, is deflected by a mirror (M1) and a beam splitter (BS1) to a position-sensitive detector (PSD) (UDT 100) that is placed in the focal plane of the lens (L). As explained above, the thermal gradients in the fluid lead to a displacement $(\Delta x, \Delta y)$ of the light distribution barycentre on the detector surface. In this configuration, this displacement is related to the deflection angles through the expressions $\Delta x = f\theta_x$, $\Delta y = f\theta_y$, where $f\,(= 1$ m) denotes the focal length of the lens (L). This displacement is converted by the PSD into a voltage signal for both directions. These signals go to specific electronics that amplifies and normalizes them with respect to the total intensity reaching the PSD, thus compensating for the fluctuations of the laser intensity. The electronic output voltages (V_x, V_y) are related with $(\Delta x, \Delta y)$ simply by the relations $V_x = A\Delta x$, $V_y = A\Delta y$, where $A = 3.94$ V mm^{-1}. By using the water parameters in table 1, the expressions for Δx and Δy and (3.1), we can write the following expressions:

$$V_x = B\langle\partial T/\partial x\rangle_z, \quad V_y = B\langle\partial T/\partial y\rangle_z \tag{3.2}$$

with $B = 2.06$ V cm K^{-1}.

The last part of the system includes the data acquisition based on two 12-bit-resolution AD converters (Burr-Brown, ADC803) interfaced with a personal computer (PC) Olivetti M-24, that samples and stores both V_x and V_y signals. The data acquisition is synchronized with the sweep by sending to the PC two pulses that mark, respectively, the beginning of the raster scan and the start of every horizontal sweep. Frames of 128 horizontal lines of 128 points each are obtained on a square area of $4.9 \times 4.9\,\mathrm{cm}^2$. The problem of errors of this technique has been discussed elsewhere (Ciliberto *et al.* 1985). We just note that the overall accuracy of the single-point measurements is about 5% and the sensitivity is about $0.02\,\mathrm{K\,cm}^{-1}$.

In every run the horizontal scanner was driven at a frequency of 40 Hz allowing us to take a whole image in about 3 s. This time is much smaller than the horizontal diffusion time $\tau_h = 2.45$ h that characterizes the motions of the convective pattern in the (x, y)-plane. Therefore, many frames (more than 100) can be taken in a interval of time $\tau_h/20$. By averaging these images the noise is reduced. It is also important to notice that under our experimental conditions (thin layer, high thermal gradient) the heating due to the laser radiation is negligible because the laser power is less than 0.5 mW and the absorption coefficient of water is small at the He-Ne laser frequency.

The laser deflection technique allows us to obtain the horizontal temperature gradient field $(\langle \partial T/\partial x \rangle_z, \langle \partial T/\partial y \rangle_z)$ averaged on the vertical coordinate. This field can be integrated numerically to recover the horizontal temperature field $\langle T \rangle_z(x, y)$. To do this integration we used the properties of a Fourier transform by means of which it was also possible to compute the spatial Fourier spectrum of $\langle T \rangle_z(x, y), S(k_x, k_y)$. We used the Cooley–Tuckey FFT algorithm, Ramírez 1985). Therefore, $\langle T \rangle_z$ may be rewritten in terms of the ψ_k, defined in (2.2)–(2.3), as

$$\langle T \rangle_z = \frac{\Delta T_c}{R_c} \langle \theta_0 \rangle_z \left[\frac{R_c}{\langle w_0 \theta_0 \rangle_z} \right]^{\frac{1}{2}} \sum_k \psi_k \exp(\mathrm{i}\boldsymbol{k} \cdot \boldsymbol{r}), \tag{3.3}$$

where the ψ_k are now obtained from the measured temperature field.

3.3.3. *Calorimetric technique*

The heat transfer across the convective cell is measured by means of a standard calorimetric technique. The convective threshold, characterized by a 'break' in the slope of the heat transfer curve as a function of the temperature difference, can also be determined. As we will see in the next section, this technique is complementary to the laser deflection technique, because in the latter the measures of the heat flow are more sensitive to the structure of the convective pattern and less to the influence of the lateral wall of the cell than the calorimetric technique.

The total heat flow q_{tot}, through the fluid layer comes from two contributions: conduction and convection, $q_{tot} = q_{conv} + q_{cond}$. The conductive part can be simply obtained from the Fourier law $q_{cond} = \lambda_w \Delta T_w/d$, where ΔT_w is the temperature difference across the fluid layer and λ_w the thermal conductivity of water. The total temperature difference across the cell is measured with two thermistors (Th2) and (Th3) (see figure 2), one placed on the upper surface of the sapphire plate and the other in the midplane of the copper plate. ΔT_w is related to the temperature difference on the sapphire ΔT_w and on the copper plate ΔT_c by the relation $\Delta T_{tot} = \Delta T_s + \Delta T_w + \Delta T_c$. Taking into account the continuity of the heat flow through the fluid layer, the sapphire and the copper plate, we have

$$q_{tot} = \lambda_c \Delta T_c/d_c = \lambda_s \Delta T_s/d_s = \lambda_w \Delta T_w/d + q_{conv}, \tag{3.4}$$

where the subscripts c and s indicate the copper and the sapphire parameters, respectively. Therefore, ΔT_w becomes

$$\Delta T_w = \frac{\Delta T_{tot} - (d_s/\lambda_s + d_c/\lambda_c)\, q_{conv}}{1 + \lambda_w d_s/\lambda_s d + \lambda_w d_c/\lambda_c d}. \tag{3.5}$$

The power P dissipated by the electrical resistor (ER) (see figure 2) heating the copper plate is determined from the value of the voltage applied, V, to the ER and by the value of the current intensity I flowing in ER, $P = IV$. However, only the fraction c_1 of P contributes to the total heat flow q_{tot} through the fluid layer, mainly due to the heat losses on the lateral walls. Calling the area of the cell S, we can write

$$q_{tot} = c_1 \frac{P}{S}, \tag{3.6}$$

and from (3.4)–(3.6) the convective heat flow q_{conv} can be written in the form

$$q_{conv} = c_1 \frac{P}{S}\left(1 + \frac{\lambda_w d_s}{\lambda_s d} + \frac{\lambda_w d_c}{\lambda_c d}\right) - \left(\frac{\lambda_w}{d}\right)\Delta T_{tot}. \tag{3.7}$$

The value of $c_2 (c_2 = c_1 d/S)$ can be directly determined from (3.7) by a best fit of measurements taken in the purely conductive state ($q_{conv} = 0$). The obtained value is $c_2 = (222.4 \pm 0.4) \times 10^{-6}\ \mathrm{mm}^{-1}$. From (3.5)–(3.7) we can also obtain the Nusselt number N

$$N = \frac{q_{tot}}{q_{cond}} = \frac{c_2 P}{\lambda_w [\Delta T_{tot} - (d_s/\lambda_s + d_c/\lambda_c)\, c_2 P/d]}. \tag{3.8}$$

All the terms in this final expression are directly measurable except the thermal conductivities, which are obtained from Weast (1985). Uncertainties in the determination of the Nusselt number N by this method were normally dominated by (*a*) the thermal fluctuations of the thermal stabilization system, (*b*) the nonlinearities in the Fourier law and (*c*) the errors in the determination of d, d_s, d_c, c_2, λ_s, λ_c, λ_w, P and ΔT. Adding these contributions, the resulting error in the Nusselt number N is about 2%.

3.4. *Experimental procedure*

To obtain experimental results with the techniques described in §3.3 we proceed as follows. The voltage applied to the heating resistance in the bottom plate is increased automatically by steps of 0.2 V. (This leads to a small change in the temperature difference, that for each voltage can be determined in stationary conditions.) After 5 h ($\approx 2\tau_h$), a time sufficient to obtain a well established pattern, the image and data acquisition start. The procedure is repeated for 30 increasing voltage values and then for 30 decreasing values. Now we present the main results obtained from these measurements.

4. Experimental results

4.1. *Experimental observations of the hexagon–roll transition*

4.1.1. *Shadowgraph technique*

Using the shadowgraph technique described in §3.3.1, pictures corresponding to a top view of the pattern were obtained. Below threshold a pattern of concentric convective rolls is visible but with a weak intensity. We have observed that in a convective cell with a triangular lateral wall these concentric rolls are less stable than

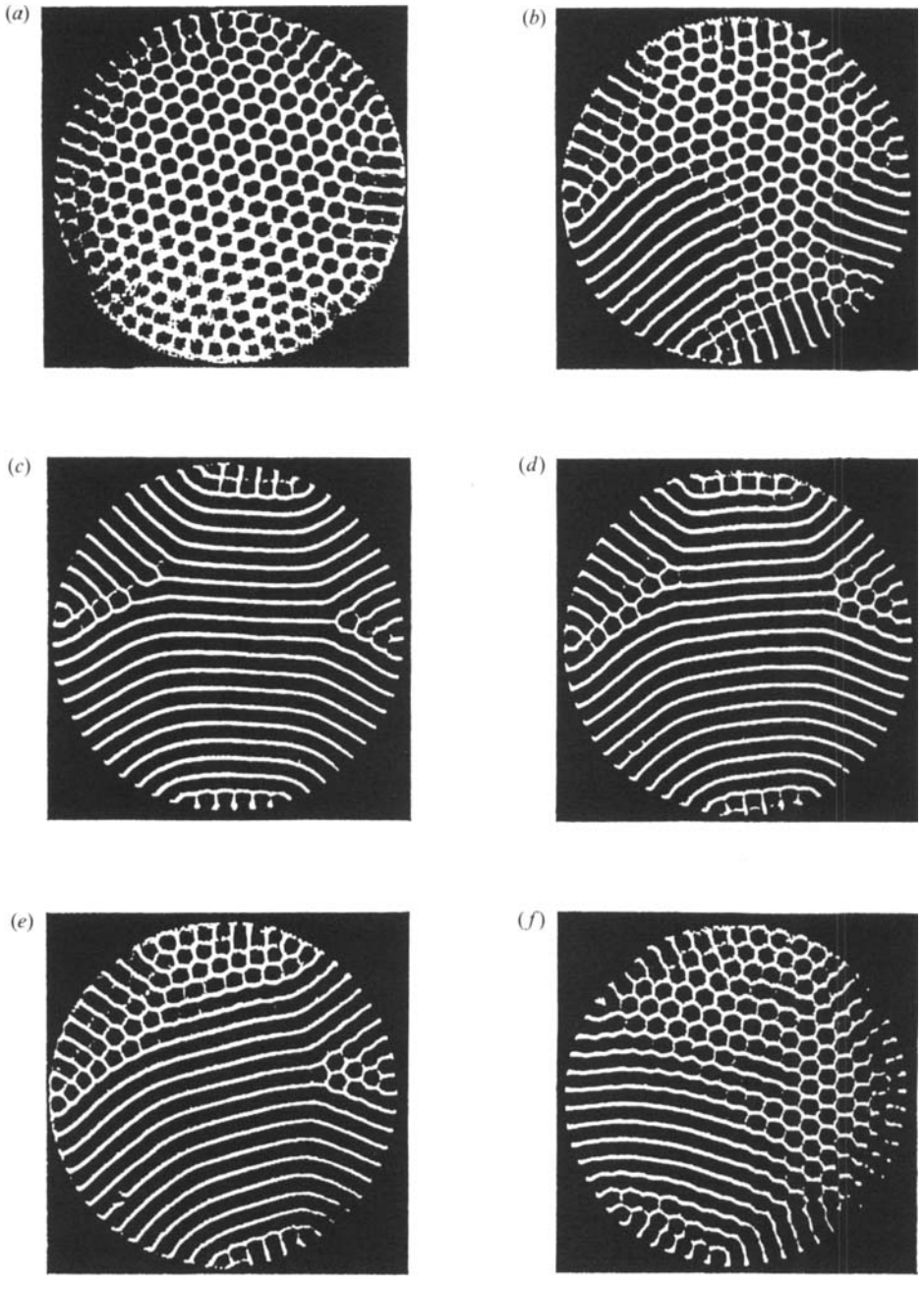

FIGURE 4. Shadowgraph images of convective pattern: (*a*) $\epsilon = 0.015$; (*b*) $\epsilon = 0.035$; (*c*) $\epsilon = 0.140$; (*d*) $\epsilon = 0.110$; (*e*) $\epsilon = 0.050$; (*f*) $\epsilon = 0.035$.

in cells with a vertical wall. This suggests that these subcritical rolls are due to a mismatch between the heat conductivities of the lateral wall and of the fluid, which causes the appearance of an horizontal temperature gradient when ΔT is changed (Meyer, Ahlers & Cannell 1987).

Pictures in figure 4 show the pattern evolution when ϵ increases above threshold. In figure 4(*a*) ($\epsilon = 0.015$) a very regular hexagonal pattern appears. Notice that a

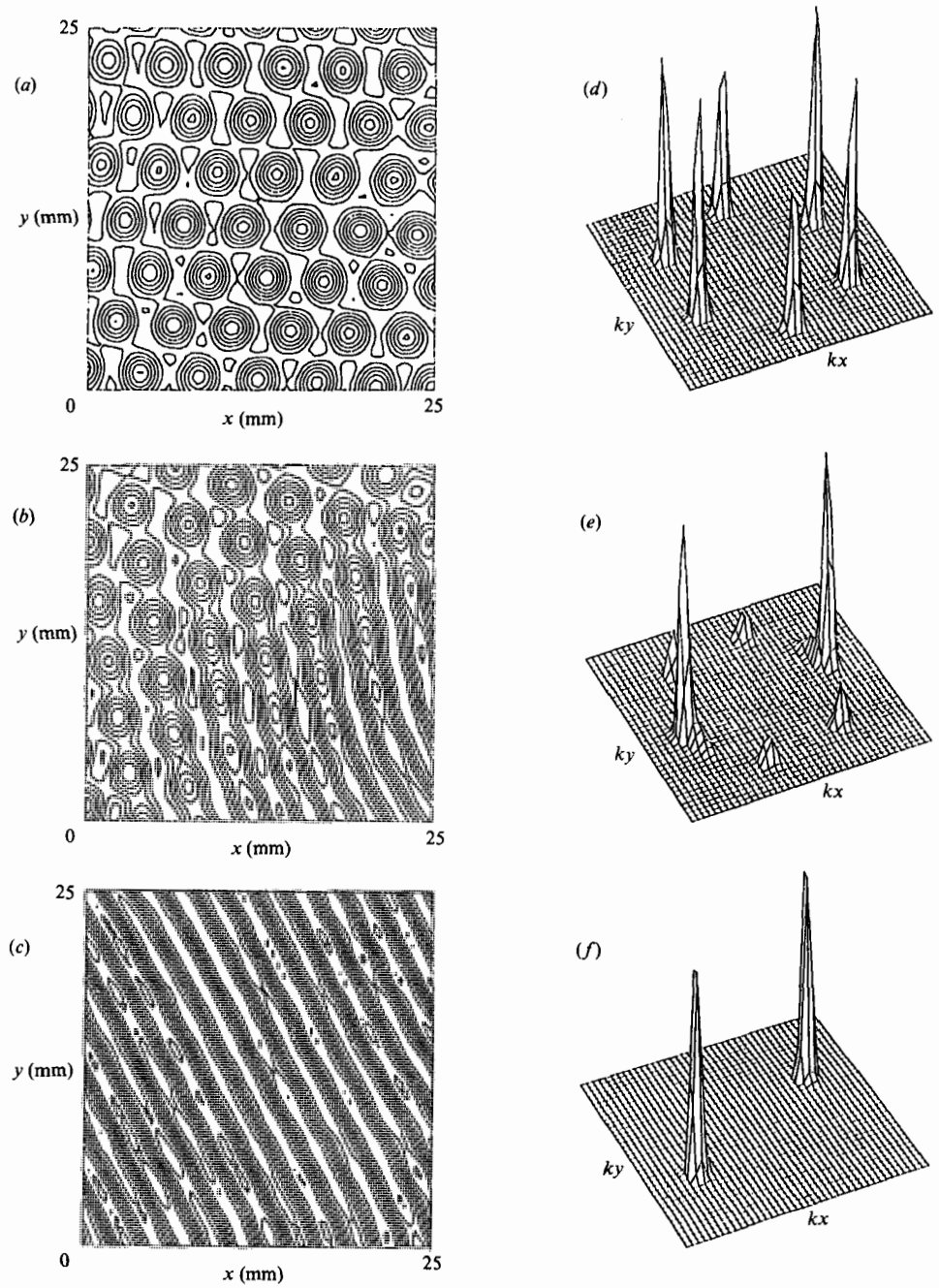

FIGURE 5. (*a–c*) Temperature-field isotherms obtained with the laser beam deflection technique for increasing ϵ (δT is the temperature difference between two isotherms): (*a*) $\epsilon = 0.022$ ($\delta T = 0.21$ K); (*b*) $\epsilon = 0.041$ ($\delta T = 0.32$ K); (*c*) $\epsilon = 0.140$ ($\delta T = 0.42$ K). (*d–f*) Fourier spectra of the temperature field in the full scanning area for the same values of ϵ as in (*a–c*) respectively.

region exists in which the intensity is weaker than in the rest of the cell. This can be due to two effects: (i) a very small difference in the layer depth due to non-perfect parallelism of the sapphire and copper plates of the cell (a difference of 10 μm suffices to create this inhomogeneity); (ii) a temperature difference between the inlet and

outlet of the refrigeration water of the upper plate due to the high heating power of the bottom plate. It is not easy to avoid these problems (i) because it is difficult to ensure a precision of less than 10 μm height in a cell of these characteristics and (ii) because we need a relatively high heating power to have convection in a very shallow cell. However, we suspect that in the present experiment the second effect is dominant. In fact, when the sense of circulation of the water in the refrigeration circuit is reversed the less intense part moves so as to remain in the region near the outlet of the cooling water.

Figure 4(*a*) also shows that the orientation of the hexagonal pattern cannot be fully compatible with the cylindrical cell geometry. On the boundary, in fact, convective motions organize themselves to form rolls perpendicular to the lateral wall. However, all the roll orientations in a cylindrical cell are not compatible with those of the three systems of rolls that form the initial hexagonal pattern. So, some lateral rolls not oriented in the same direction as the three main sets of rolls that form the hexagonal pattern appear in six regions. (By analogy with solid state physics these can be considered as *frustration* regions.) In the subsequent evolution (see figure 4*b*, $\epsilon = 0.035$) these rolls invade the cell. The three orientations compete till, after some transitions, one of the orientations prevails. Hereafter a regular pattern of rolls is established as can be seen in figure 4(*c*) ($\epsilon = 0.140$). In figure 4(*c*) one can see that some grain boundaries exist where the hexagonal symmetry still survives. The stability of the structures shown in these figures has been checked at least for 50 h (that in figure 4*c* for more than 140 h).

In figures 4(*d*) ($\epsilon = 0.110$), 4(*e*) ($\epsilon = 0.050$), and 4(*f*) ($\epsilon = 0.035$) the evolution of the pattern with decreasing ϵ is shown. From this sequence one sees that hexagons invade the pattern of rolls from the grain boundaries till the initial, almost perfect, pattern of hexagons (like that in figure 4*a*) is recovered. Finally, from these pictures it is possible to determine the wavenumbers k for the different patterns. No difference between hexagon and roll patterns has been found: the common value is $k_c = 3.1 \pm 0.05$.

4.1.2. *Reconstruction of the temperature field with the laser deflection technique*

The deflection technique gives, with great accuracy, local quantitative information that can be integrated to determine the global characteristics of the pattern. Figure 5 show the isotherms of the temperature field $\langle T \rangle_z(x, y)$ at different values of ϵ, reconstructed as explained in §3.3.2. We report on a central square (24.5×24.5 mm) of the whole scanning area (49×49 mm) in order to show the details of the temperature field. The corresponding Fourier spectra $S(k_x, k_y)$ computed over the whole scanning area are also gathered in figure 5. In figure 5(*d*) the regularity of the hexagonal pattern is well reflected in the six sharp peaks in the spectrum. The sequence with increasing ϵ shows the destabilization of this hexagonal pattern. One of the three set of rolls that forms the hexagonal pattern prevails, as it can be seen in figure 5(*b*) and in the corresponding spectra, figure 5(*e*). Then a single set of rolls is well established (figure 5*c*, *f*). With decreasing ϵ, an inverse process takes place (figure 6). At some points two sets of rolls, oblique to the main one, reappear leading finally, for small values of ϵ, to a regular pattern of hexagons like the initial one. (As we will see below this process is hysteretic and the transition threshold can be determined with this technique).

From the temperature field one can calculate the wavenumber of the pattern which in all the cases analysed is $k_c = 3.1 \pm 0.05$, in good agreement with that obtained with the shadowgraph technique.

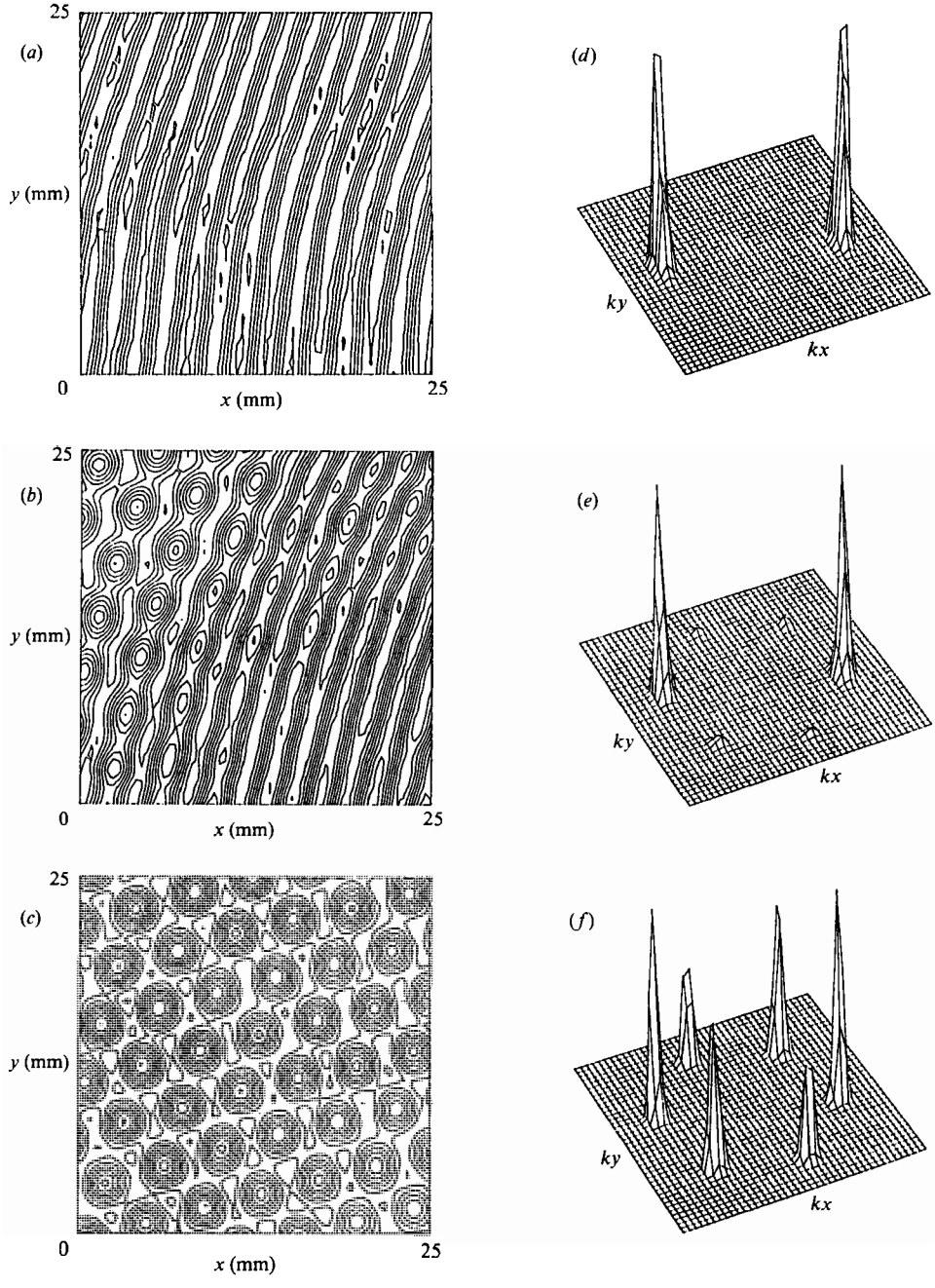

FIGURE 6. (*a–c*) Temperature-field isotherms obtained with laser beam deflection technique for decreasing ϵ: (*a*) $\epsilon = 0.086$ ($\delta T = 0.42$ K); (*b*) $\epsilon = 0.033$ ($\delta T = 0.21$ K); (*c*) $\epsilon = 0.027$ ($\delta T = 0.21$ K). (*d–f*) Fourier spectra of the temperature field in the full scanning area for the same values of ϵ as in (*a–c*) respectively.

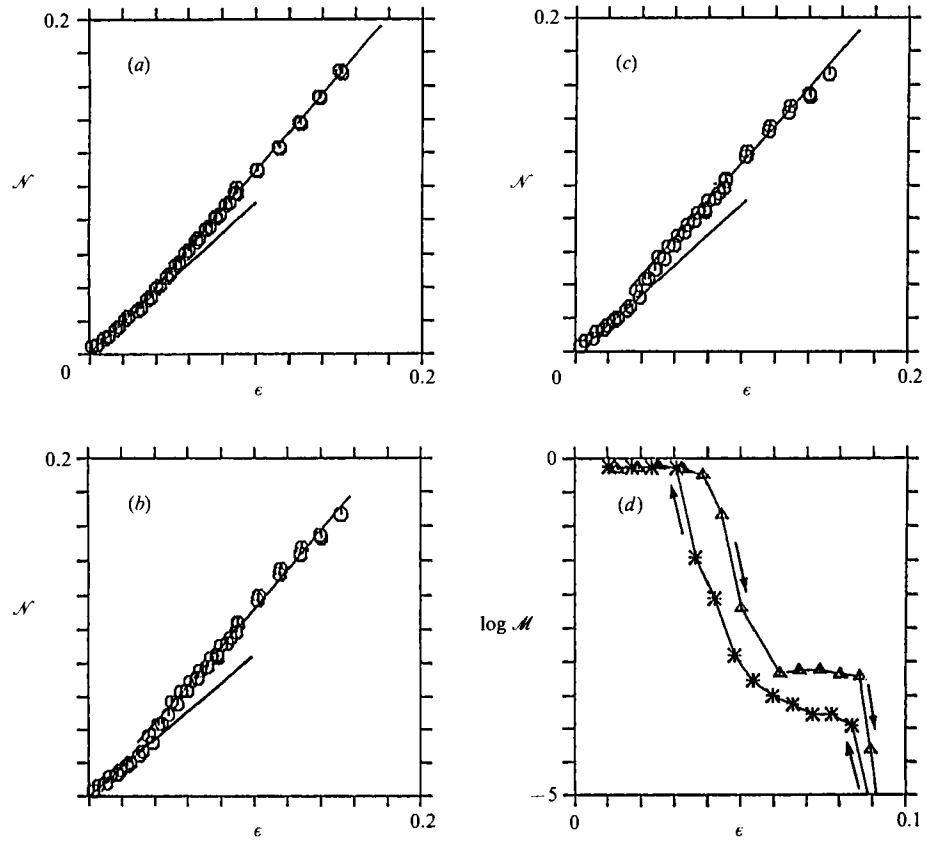

FIGURE 7. Non-dimensional heat flow $\mathcal{N} = (N-1)R/R_c$ as a function of ϵ. (*a*) Calorimetric technique (linear fit). Laser beam deflection technique: (*b*) linear fit, (*c*) nonlinear fit. (*d*) Normalized sum $\mathcal{M}$ of square amplitudes of the two modes $\langle|A_2|^2\rangle_{x,y}$, $\langle|A_3|^2\rangle_{x,y}$ at $\frac{2}{3}\pi$ rad with respect to the surviving mode $\langle|A_1|^2\rangle_{x,y}$ as a function of ϵ. The arrows indicate the different evolution of the vanishing modes when ϵ increases or decreases.

4.2. *Heat flow measurements*

The heat flow across the convective cell is determined using the two methods, calorimetric and laser beam deflection, described in §§3.3.2 and 3.3.3.

4.2.1. *Calorimetric technique*

From experimental data, the non-dimensional convective heat flow $\mathcal{N}$ as a function of T can be determined. These data are well fitted with two straight lines with different slopes, which correspond to patterns of hexagons and rolls, respectively. By extrapolation of these straight lines to $\mathcal{N} \to 0$ (that is $N \to 1$) we can obtain the temperature difference at threshold. The values are

$$\left.\begin{aligned} \Delta T_c &= 12.60 \pm 0.02\,\text{K} \quad \text{(hexagons)}, \\ \Delta T_c &= 12.68 \pm 0.02\,\text{K} \quad \text{(rolls)}. \end{aligned}\right\} \tag{4.1}$$

(Note: the errors in (4.1) are smaller than the errors in N because they depend only on the experimental accuracy. Indeed ΔT_c can be obtained by a best fit of P versus ΔT. The errors reported here are those arising from this fit.)

The main results are shown in figure 7(*a*), where $\mathcal{N}$ is represented as a function of ϵ. (As we will discuss in the following the best choice of ΔT_c to define ϵ is

$\Delta T_c = 12.62$ K.) The straight lines in this diagram have slopes η_h ($\approx \mathscr{R}_h^{-1}$) $= 0.89 \pm 0.02$ for hexagons and η_r ($= \mathscr{R}_r^{-1}$) $= 1.15 \pm 0.02$ for rolls. In the conditions of the present experiment it is not possible to determine the hysteretic region (coexistence of hexagons and rolls) with this calorimetric technique.

4.2.2. *Laser deflection technique*

The non-dimensional convective heat flow $\mathscr{N}$ can also be obtained simply by adding the intensity of the modes (see (2.11)). A linear fit of these data has been made. But as one can see in (A 7) or (2.12) this cannot be exact for hexagons near threshold. For hexagons, therefore we have also fitted with a function in the form

$$\Delta T \mathscr{N}^{\frac{1}{2}} = \Delta T_c \mathscr{N}^{\frac{1}{2}} + \Delta T_c \mathscr{N} \mathscr{P} / R_c^{\frac{1}{2}} + \Delta T_c \mathscr{N}^{\frac{3}{2}} \mathscr{R}_h + I_b \sqrt{3}\, \Delta T_c, \tag{4.2}$$

with $\mathscr{P} = a(\frac{1}{3}R_c)^{\frac{1}{2}}$, $\mathscr{R}_h = \frac{1}{3}C$, $\mathscr{R}_r = c$ (see also the Appendix and (2.12)–(2.13)). Equation (4.2) comes from the amplitude equations with a term I_b that takes into account the contributions of the lateral wall and the imperfections of the cell. Because of this fact the bifurcation is imperfect (Newell 1979). For rolls the function taken is

$$\Delta T_c^{\frac{3}{2}} \mathscr{N} = (\Delta T - \Delta T_c)/\mathscr{R}_r ((\Delta T_c)^{\frac{1}{2}} + D(\Delta T - \Delta T_c)^{\frac{1}{2}}), \tag{4.3}$$

which comes from the expression

$$\mathscr{N} = \epsilon/\mathscr{R}_r (1 + D\epsilon^{\frac{1}{2}}), \tag{4.4}$$

where the term in $\epsilon^{\frac{1}{2}}$ is the first corrective term to the non-dimensional convective heat flow $\mathscr{N}$ (Niederlander, Lücke & Kamps 1988) and D is a parameter to be determined by the fitting.

The two straight lines of the linear fit obtained with this technique are shown in figure 7 (*b*). By extrapolation of the straight lines to $\mathscr{N} \to 0$ we obtain the temperature difference at threshold. The values are

$$\left.\begin{aligned} \Delta T_c &= 12.62 \pm 0.03 \text{ K} \quad \text{(hexagons)}, \\ \Delta T_c &= 12.62 \pm 0.02 \text{ K} \quad \text{(rolls)}, \end{aligned}\right\} \tag{4.5}$$

while, by fitting the experimental points in figure 7 (*c*) with the expressions (4.2) and (4.4) we obtain the values

$$\left.\begin{aligned} \Delta T_c &= 12.72 \pm 0.04 \text{ K} \quad \text{(hexagons)}, \\ \Delta T_c &= 12.60 \pm 0.03 \text{ K} \quad \text{(rolls)}. \end{aligned}\right\} \tag{4.6}$$

The values obtained differ slightly. The maximum difference arises from the nonlinear hexagonal fitting. However, we do not consider this value representative because the fitting is very delicate because of the small interval of ϵ in which hexagons are stable. Therefore, by taking the average of the remaining values we have

$$\Delta T_c = 12.62 \text{ K}, \tag{4.7}$$

which will be taken as reference in the following.

The rest of the parameters in the linear fit are

$$\mathscr{R}_h = 1.16 \pm 0.03, \quad \mathscr{R}_r = 0.885 \pm 0.02. \tag{4.8}$$

The nonlinear fit gives instead

$$\left.\begin{aligned} \mathscr{R}_h = 1.14 \pm 0.05, \quad \mathscr{R}_r = 0.86 \pm 0.03, \quad \mathscr{P} = -1.30 \pm 1.33, \\ I_b = (3.1 \pm 0.2) \times 10^{-4}, \quad D = (-6.0 \pm 0.6) \times 10^{-2}. \end{aligned}\right\} \tag{4.9}$$

The large indeterminacy in the parameter $\mathscr{P}$ that accounts for the non-Boussinesq effects is because the hysteretic region near threshold ($R_a < R < R_c$) is not observable under the present conditions. However, we can conclude that there is good agreement between the values of $\mathscr{R}_h$ and $\mathscr{R}_r$ obtained with the two methods. We also notice that the imperfection parameter I_b is very small. For many purpose I_b can be neglected, but the fact that it is different from zero accounts for the influence of the lateral walls in the formation of the subcritical concentric rolls.

4.3. *Comparison between theory and experiments*

We use the value $\Delta T_c = 12.62$ K to evaluate the non-Boussinesq corrections at threshold and the normalized Rayleigh number ϵ. This critical temperature difference leads to a mean temperature $T_m = 28.3$ °C.

4.3.1. *Comparison of the critical temperature difference*

Now, after introducing the values of the fluid parameters at mean temperature T_m (see table 1) for our experimental conditions in the expression

$$\Delta T_c|_{\text{theor}} = \frac{R_c \nu(T_m)\kappa(T_m)}{\alpha(T_m) g d^3}, \tag{4.10}$$

where $R_c = 1708$, one obtains the following value:

$$\Delta T_c|_{\text{theor}} = 12.58 \text{ K}.$$

The small discrepancy between this value and the experimental one is mainly due to the indeterminacy in the liquid depth. A small variation in the depth of about $\delta d = 10$ μm leads to an indeterminacy of $\delta(\Delta T_c)_{\text{theor}} = 0.21$ K. Notice that although the absolute error in the liquid depth is very small, the relative error is about 0.6%, which gives a relative error in the temperature difference of about 1.8%.

4.3.2. *Comparison of the slopes of the convective heat flow curves*

The value of the coefficient $\mathscr{P}$ can be easily obtained when one knows the maximum and minimum temperatures in the cell at the convective threshold. The cold top plate is at 22 °C, the hot bottom plate is at 34.6 °C. Taking the values of the fluid parameters at these temperatures (see table 1) and putting them in (A 2) one obtains

$$\gamma_0 = -3.61 \times 10^{-3}, \quad \gamma_1 = -2.00 \times 10^{-1}, \quad \gamma_2 = 2.74 \times 10^{-1}, \quad \gamma_3 = -3.11 \times 10^{-2}, \quad \gamma_4 = 6.22 \times 10^{-4};$$

then, introducing the values of γ_i and P_i (see (A 3)) in (A 1) one finds

$$\mathscr{P} = -2.06. \tag{4.11a}$$

As noted in the Appendix the negative value for $\mathscr{P}$ is in agreement with the sense of circulation (upward motion in the centre) observed in the experiment. The values of ν and κ at the mean temperature T_m in table 1 lead to $Pr = 5.63$. This value is introduced in the approximated theoretical expression for the parameters $\mathscr{R}_h$ ($\approx \eta_h^{-1}$) and $\mathscr{R}_r$ ($= \eta_r^{-1}$) in Busse's theory to obtain

$$\mathscr{R}_h = 0.905, \quad \mathscr{R}_r = 0.699. \tag{4.11b}$$

The theoretical values of the slopes, η_h ($\approx \mathscr{R}_h^{-1}$) and η_r ($= \mathscr{R}_r^{-1}$), of the convective heat flow curves, recovered from these expressions, and the experimental ones, recovered from (4.8) and (4.9), are reported in table 2.

Method	$\mathscr{R}_h^{-1}$	$\mathscr{R}_r^{-1}$	$\mathscr{R}_h/\mathscr{R}_r$
Theoretical	1.11	1.43	1.29
Calorimetric	0.89 ± 0.02	1.15 ± 0.02	1.29 ± 0.05
Optical (lin.)	0.86 ± 0.03	1.13 ± 0.02	1.31 ± 0.06
Optical (nonlin.)	0.88 ± 0.04	1.16 ± 0.04	1.32 ± 0.10

TABLE 2. Theoretical and different experimental values of $\mathscr{R}_h^{-1}$, $\mathscr{R}_r^{-1}$ and $\mathscr{R}_h/\mathscr{R}_r$

Method	a	b	c
Theoretical	8.63×10^{-2}	1.01	0.70
Calorimetric	—	1.25 ± 0.05	0.87 ± 0.02
Optical (lin.)	—	1.30 ± 0.06	0.89 ± 0.02
Optical (nonlin.)	—	1.28 ± 0.09	0.86 ± 0.03

TABLE 3. Values of the different parameters in the amplitude equations (2.7) obtained by different methods (see the text)

One can see that the experimental slopes η_h and η_r are smaller than the theoretical ones. This is due to finite-size effects in the experimental system (Ahlers *et al.* 1981). These finite-size effects reduce the convective heat flow, but by the same factor for hexagons and rolls (Walden & Ahlers 1981). This is confirmed by the fact that both the theoretical and the experimental ratios between the slopes are almost the same. Another remarkable fact is the good agreement between the calorimetric and the optical measurements, which confirms the validity of the construction used to calculate the heat flow with the laser deflection technique.

The values (4.11*a*, *b*) and (A 9) provide the theoretical values of the coefficients in the amplitude equations (2.7). Also, from (2.12) and (2.13) one can recover the corresponding experimental coefficients. The values of those theoretical and experimental coefficients are reported in table 3.

4.3.3. *Comparison of the transition threshold*

The images obtained with the shadowgraph and the laser deflection technique indicate that the transition from hexagons to rolls is not homogeneous. The finite size has a very considerable influence, as we have seen in the heat flow measurements.

With the calorimetric technique it is not possible to see clearly the transition from hexagons to rolls and vice versa. Therefore, we have to utilize only the experimental results obtained with the laser deflection technique demonstrate this transition. With this technique we can determine the square amplitudes $\langle|A_i|^2\rangle_{x,y}$ of the three sets of rolls that constitute the hexagonal pattern and so we can define the following parameter:

$$\mathscr{M} = \frac{\langle|A_2|\rangle_{x,y}^2 + \langle|A_3|\rangle_{x,y}^2}{2\langle|A_1|\rangle_{x,y}^2}, \tag{4.12}$$

where A_1 is the amplitude of the surviving set of rolls, while A_2 and A_3 are the modes which disappear in the transition. In figure 7(*d*), $\log \mathscr{M}$ as a function of ϵ is shown. The arrows in this figure indicate the different evolutions of the vanishing modes when ϵ increases or decreases. As expected, the transition is smooth and hysteretic in the interval $0 \leqslant \log \mathscr{M} \leqslant -\infty$. By increasing ϵ the pattern of hexagons is not

Method	ϵ_r	ϵ_h	ϵ_h/ϵ_r
Theoretical	5.46×10^{-2}	0.188	3.44
Optical	$(3.0\pm0.1)\times10^{-2}$	0.09 ± 0.005	3.0 ± 0.3
Ph.c. (1)	$(3.9\pm1.9)\times10^{-2}$	0.134 ± 0.06	3.45 ± 0.09
Ph.c. (2)	$(3.6\pm3.2)\times10^{-2}$	0.127 ± 0.12	3.49 ± 0.16

TABLE 4. The transition thresholds with different methods. Ph.c. (phenomenological correction) (1, 2) values have been obtained after introducing the experimental values (1 = optical with linear fitting; 2 = optical with nonlinear fitting) in the formulae (2.8)–(2.10). The errors for ϵ_h, ϵ_r and ϵ_h/ϵ_r are calculated from these analytical formulae, taking the experimental errors for the coefficients b and c.

suddenly replaced by a pattern of rolls, but in a small interval of ϵ the two symmetries compete. In contrast, by decreasing ϵ the pattern of rolls is smoothly replaced by hexagons that grow from the grain boundaries, as one can see in the sequence of photos in figure 4 (*c–f*).

The thresholds ϵ_r and ϵ_h for the transitions and their ratio ϵ_h/ϵ_r, obtained with different methods, are reported in table 4. The two first rows indicate theoretical and experimental values. They differ by a factor about two. This discrepancy is due to different facts related to the finite size of the convective cell. As we have stressed in the present work, the analysis of Busse (1967*a*) has some limitations (validity for an infinite system, undeterminacy in the value of $\mathscr{P}$ as a function of Pr in the rigid–rigid case). Therefore, one must take care when comparing the experimental values of the thresholds with the theoretical ones. However, as the amplitude equation formalism (§2) is not limited to an infinite system, it is possible to correct the thresholds in a coherent manner. As one can see from (2.8), (2.9) and (2.12), (2.13) the transition thresholds are linked to the heat flow for different symmetries. As a consequence it is worthwhile analysing if the decreasing of the experimental thresholds $\epsilon_{h,r}$, with respect to their theoretical values, is related to a decrease of the experimental slopes $\eta_{h,r}$. This question has been analysed in detail in a recent work (Pérez-García, Pampaloni & Ciliberto 1990*b*). Introducing in (2.8) and (2.9) the experimental values of b and c, and the theoretical value of a (we cannot experimentally determine a with sufficient precision) one obtains the values of $\epsilon_{h,r}$ reported in the last two rows in table 4 (the subscript ph.c. stand for *phenomenological corrections*). The indices (1) and (2) refer to the values obtained with the linear and the nonlinear fits, respectively. In these calculations we have taken the theoretical value of $\mathscr{P}$, because the experiment does not give this parameter with a sufficient accuracy. Moreover, one expects that $\mathscr{P}$ is less influenced by the finite-size effect than the other parameters. The results show that the values of $\eta_{h,r}$, obtained in this experiment, are consistent with a decrease in the threshold values $\epsilon_{h,r}$, with respect to those for an infinite system. Moreover, the thresholds corrected in this phenomenological manner are nearer to the experimental ones than those calculated theoretically. From (A 9) it is obvious that the parameter a is linearly dependent on $\mathscr{P}$. The nonlinear fit (4.2) gives $\mathscr{P}_{exp} = -1.30$ (smaller than that calculated theoretically $\mathscr{P}_{theor} = -2.06$), but this value is affected by a great uncertainty.

Even with these phenomenological corrections the experimental and theoretical values cannot be in complete agreement. The reason is that the corrections are made by means of some global parameters ($\mathscr{R}_{h,r}$) that do not account for the particular details of the pattern, and more specifically, for the defects that, as seen in photographies, are very important to nucleate the transition (Ciliberto *et al.* 1990).

5. Summary and conclusions

We list here the main results and conclusions of our investigation:

(1) We have extended previous experimental and theoretical works on convection under non-Boussinesq conditions.

(2) A laser beam deflection technique has been used. This is a more powerful technique than the calorimetric one because it allows, apart from a global quantity such as the heat flow, a local measure of the temperature field to be obtained, by which one can also study the defects of the convective structure. Moreover, this technique allows qualitative features of the convective texture to be obtained that are in perfect agreement with the shadowgraph ones.

(3) We have shown that Busse's (1967) analysis gives the same results as the amplitude equations in the case of an infinite system. The last formalism is more general than the previous one because it includes spatial variations of the convective structure, for instance, like those due to the finite-size effects or to the presence of defects.

(4) By the Fourier analysis of the convective temperature field we have been able to determine the slow varying amplitude of the spatial modes that constitute the pattern and, therefore, to characterize the hysteresis of the hexagon–roll transition more accurately than in previous works.

(5) A stable coexistence of hexagons and rolls, not theoretically predicted, has been observed.

(6) We have done a comparison of the experimental results with the theoretical ones of Busse's analysis, demonstrating that the discrepancies are just due to finite-size effects. These effects have been widely studied in Rayleigh–Bénard convection but not in the non-Boussinesq case.

(7) An important conclusion is that the finite-size effects, and the defects (Ciliberto *et al.* 1990) induced by these, are crucial in this kind of transition.

(8) From the present analysis it is evident that the transition between different symmetries has many similarities with the nucleation process in the first-order phase transition in a thermal equilibrium system.

We have benefited from discussions with G. Ahlers, F. T. Arecchi, P. Coullet, P. Hohenberg, J. Lega, M. Lücke. This work has been partially supported by a EEC grant SCI-0035-C, by the Gruppo Nazionale di Struttura della Materia (Italy), by the DGICYT of the Spanish Government (CE-0002-89) and by an Italy–Spain Integrated Action (n°46-1989, n°48-1990).

Appendix

We recall briefly the main results of Busse's (1967*a*) analysis.

The departures from the Oberbeck-Boussinesq (OB) approximation are quantitatively given by a parameter $\mathscr{P}$, defined as

$$\mathscr{P} = \sum P_i \gamma_i, \tag{A 1}$$

where

$$\gamma_0 = -\frac{(\rho_1 - \rho_2)}{\rho}, \quad \gamma_1 = \frac{\alpha_1 - \alpha_2}{2\alpha}, \quad \gamma_2 = \frac{\nu_1 - \nu_2}{\nu}, \quad \gamma_3 = \frac{\lambda_1 - \lambda_2}{\lambda}, \quad \gamma_4 = \frac{C_{p1} - C_{p2}}{C_p}.$$

(A 2)

Here the subscripts 1 and 2 refer to the values at the bottom and at the top of the cell, respectively. Their differences are normalized by the value of the corresponding parameters at the mean temperature $T_m = \frac{1}{2}(T_1 + T_2)$. The coefficients P_i are

$$P_0 = 2.676 - \frac{0.158}{Pr}, \quad P_1 = -6.603 - \frac{0.5023}{Pr}, \quad P_2 = 2.755, \quad P_3 = 2.917 - \frac{0.5023}{Pr},$$

$$P_4 = -6.229 + \frac{0.2512}{Pr}. \tag{A 3}$$

(We take the values obtained by Busse 1967*a* for $Pr = \infty$ in the rigid–rigid case, adding the corrections for finite Pr in the free–free case, Ahlers 1980).

These departures from the OB approximation give rise to the following consequences: (i) near threshold the pattern is hexagonal; (ii) subcritical motions are possible; (iii) an hysteretic transition between hexagons and rolls is predicted, when the heating increases. Therefore the bifurcation is *transcritical* as indicated in figure 1, and several threshold values can be distinguished:

$$R_a \leqslant R_c \leqslant R_r \leqslant R_h. \tag{A 4}$$

Depending on the previous history of R, between $R_a \leqslant R \leqslant R_c$ both hexagons and conduction can exist; in the interval $R_c \leqslant R \leqslant R_r$ only hexagons are stable; between $R_r \leqslant R \leqslant R_h$, both hexagons and rolls can exist; for $R \geqslant R_h$ only rolls are stable. These thresholds depend on $\mathscr{P}$ as

$$R_a = R_c - \frac{\mathscr{P}^2}{4\mathscr{R}_h}, \quad R_r = R_c + \frac{3\mathscr{R}_r \mathscr{P}^2}{\mathscr{L}_2^2}, \quad R_h = R_c + \frac{(9\mathscr{R}_h - 3\mathscr{L}_2)\mathscr{P}^2}{\mathscr{L}_2^2}, \tag{A 5}$$

with

$$\left.\begin{aligned} \mathscr{R}_h &= 0.89360 + 0.04959 Pr^{-1} + 0.06787 Pr^{-2}, \\ \mathscr{R}_r &= 0.69942 - 0.00472 Pr^{-1} + 0.00832 Pr^{-2}, \\ \mathscr{L}_2 &= 0.29127 + 0.08147 Pr^{-1} + 0.08933 Pr^{-2}. \end{aligned}\right\} \tag{A 6}$$

Notice that, at fixed Pr, these thresholds depend on $\mathscr{P}$ only. The sign of $\mathscr{P}$ determines the sense of circulation in hexagonal cells: the motion is upward in the centre and downward on the sides of each hexagon for negative $\mathscr{P}$, while it is in the opposite sense for positive $\mathscr{P}$ (Busse 1967*a*). The expressions for the heat flow are the following (Ahlers 1980):

$$\mathscr{N}_h = \frac{1}{\mathscr{R}_h}\left[\frac{\mathscr{P}^2}{2R_c\mathscr{R}_h} + \epsilon + \frac{\mathscr{P}}{2R_c^{\frac{1}{2}}}\left\{\frac{P^2}{R_c\mathscr{R}_h^2} + \frac{4\epsilon}{\mathscr{R}_h}\right\}^{\frac{1}{2}}\right] \tag{A 7}$$

in the case of hexagons, while for rolls

$$\mathscr{N}_r = \epsilon/\mathscr{R}_r. \tag{A 8}$$

A direct comparison among (A 7), (A 8) and (2.12), (2.13) allows the relation among (A 5) and (2.8), (2.9) for the transition thresholds to be determined (Pérez-García *et al.* 1990*a*):

$$a^2 = 3\mathscr{P}^2/R_c, \quad b = \tfrac{1}{2}(3\mathscr{R}_h - \mathscr{R}_r), \quad c = \mathscr{R}_r, \quad \mathscr{L}_2 = (b - c). \tag{A 9}$$

Notice that this identification leads also to the expression $\mathscr{L}_2 = \frac{3}{2}(\mathscr{R}_h - \mathscr{R}_r)$, whose validity can be directly checked from (A 6).

REFERENCES

AHLERS, G. 1980 *J. Fluid Mech.* **98**, 137.

AHLERS, G., CROSS, M., HOHENBERG, P. C. & SAFRAN, S. 1981 *J. Fluid Mech.* **110**, 297.

BEHRINGER, R. P. & AHLERS, G. 1982 *J. Fluid Mech.* **125**, 219.

BROWN, S. N. & STEWARTSON, K. 1977 *Stud. Appl. Maths* **57**, 187.

BUSSE, F. H. 1967*a* *J. Fluid Mech.* **30**, 625.

BUSSE, F. H. 1967*b* *J. Math. Phys.* **46**, 140.

BUSSE, F. H. & RIAHI, N. 1980 *J. Fluid Mech.* **96**, 243.

CATTON, I. 1970 *Trans ASME* C: *J. Heat Transfer* **92**, 186.

CHANDRASEKHAR, S. 1961 *Hydrodynamic and Hydromagnetic Stability*. Clarendon.

CHARLSON, G. S. & SANI, R. L. 1970 *Intl J. Heat Mass Transfer* **13**, 1479.

CILIBERTO, S., COULLET, P., LEGA, J., PAMPALONI, E. & PÉREZ-GARCÍA, C. 1990 *Phys. Rev. Lett.* **65**, 2370.

CILIBERTO, S., FRANCINI, F. & SIMONELLI, F. 1985 *Optics Commun.* **54**, 381.

CILIBERTO, S., PAMPALONI, E. & PÉREZ-GARCÍA, C. 1988 *Phys. Rev. Lett.* **61**, 1198.

CROSS, M. 1980 *Phys. Fluids* **23**, 1727.

CROSS, M., DANIELS, P. G., HOHENBERG, P. & SIGGIA, E. D. 1980 *Phys. Rev. Lett.* **45**, 898.

DAVIS, S. H. 1967 *J. Fluid Mech.* **30**, 465.

DAVIS, S. H. & SEGEL, L. A. 1968 *Phys. Fluids* **11**, 470.

DAVIS-JONES, R. 1970 *J. Fluid Mech.* **127**, 155.

DUBOIS, M., BERGÉ, P. & WESFREID, J. E. 1978 *J. Phys. Paris* **39**, 1253.

GIGLIO, M. & VENDRAMINI, A. 1975 *Phys. Rev. Lett.* **34**, 561.

GIGLIO, M. & VENDRAMINI, A. 1977 *Phys. Rev. Lett.* **38**, 26.

HEINRICHS, R., AHLERS, G. & CANNELL, D. S. 1987 *Phys. Rev.* A**35**, 2761.

HEUTMAKER, M. S. & GOLLUB, J. P. 1987 *Phys. Rev.* A**35**, 242.

HOARD, C. Q., ROBERTSON, C. R. & ACRIVOS, A. 1970 *Intl J. Heat Mass Transfer* **13**, 849.

JENKINS, D. R. & PROCTOR, M. R. E. 1984 *J. Fluid Mech.* **139**, 461.

KOSCHMIEDER, E. L. & CAMPBELL, J. R. 1987 Onset of Rayleigh–Bénard convection in thin fluid layers. Preprint.

LUIJKX, J. M. & PLATTEN, J. K. 1981 *J. Non-Equilib. Thermodyn.* **6**, 141.

MANNEVILLE, P. 1990 *Dissipative Structures and Weak Turbulence*. Academic.

MEYER, C. W., ALHERS, G. & CANNELL, D. 1987 *Phys. Rev. Lett.* **59**, 1577.

NEWELL, A. C. 1979 In *Pattern Formation and Pattern Recognition* (ed. H. Haken), p. 244. Springer.

NEWELL, A. C. & WHITEHEAD, J. A. 1969 *J. Fluid Mech.* **38**, 279.

NIEDERLÄNDER, J., LÜCKE, M. & KAMPS, M. 1991 *Z. Phys.* B **82**, 135.

PALM, E. 1960 *J. Fluid Mech.* **8**, 183.

PALM, E., ELLINGSEN, T. & GJEVIK, B. 1967 *J. Fluid Mech.* **30**, 651.

PANTALONI, J. & CERISIER, P. 1983 In *Cellular Structures in Instabilities* (ed. E. Wesfreid & S. Zaleski), p. 197. Springer.

PÉREZ-GARCÍA, C., PAMPALONI, E. & CILIBERTO, S. 1990*a* In *Quantitative Measures of Complex Dynamical Systems* (ed. N. B. Abraham & A. Albano), p. 405, Plenum.

PÉREZ-GARCÍA, C., PAMPALONI, E. & CILIBERTO, S. 1990*b* *Europhys. Lett.* **12**, 51.

RAMÍREZ, R. W. 1985 *The FFT Fundamental and Concepts*. Prentice Hall.

RICHTER, F. M. 1978 *J. Fluid Mech.* **89**, 553.

RIHAI, N. 1985 *J. Fluid Mech.* **152**, 113.

SCHLÜTER, A., LORTZ, D. & BUSSE, F. H. 1965 *J. Fluid Mech.* **23**, 129.

SEGEL, L. A. 1965 *J. Fluid Mech.* **21**, 359.

SEGEL, L. A. 1969 *J. Fluid Mech.* **38**, 203.

SEGEL, L. A. & STUART, J. T. 1962 *J. Fluid Mech.* **13**, 289.

SOMMERSCALES, E. F. C. & DOUGHERTY, T. S. 1970 *J. Fluid Mech.* **42**, 755.
STEINBERG, V., AHLERS, G. & CANNELL, D. S. 1985 *Physica Scr.* **32**, 534.
WALDEN, R. W. & AHLERS, G. 1981 *J. Fluid Mech.* **109**, 89.
WALDEN, R. W., KOLODNER, P., PASSNER, A. & SURKO, C. M. 1987 *J. Fluid Mech.* **185**, 205.
WEAST, R. C. (ed.) 1985 *Handbook of Chemistry and Physics*, 66th edn. CRC Press.
WESFREID, J., POMEAU, Y., DUBOIS, M., NORMAND, C. & BERGÉ, P. 1978 *J. Phys. Lett.* **39**, 725.